A 4-DoF wearable hand device for haptic rendering of surfaces and edges

A 4-DoF Wearable Hand Device for Haptic Rendering of Surfaces and Edges

Lisheng Kuang[a], Monica Malvezzi[b], Marco Ferro[a], Domenico Prattichizzo[b,c], Paolo Robuffo Giordano[a], Francesco Chinello[d], Claudio Pacchierotti[a]

[a] *CNRS, Univ Rennes, Inria, IRISA, 263 Avenue General Leclerc, Rennes, 35000, France*
[b] *University of Siena, Via Banchi di Sotto, 55, Siena, 53100, Italy*
[c] *Italian Institute of Technology, Via Morego, 30, Genova, 16163, Italy*
[d] *Aarhus University, Birk Centerpark 15, Herning, 7400, Denmark*

Abstract

We present a 4-degrees-of-freedom (4-DoF) wearable haptic device for the palm, able to provide the sensation of interacting with slanted surfaces and edges. It is composed of a static upper body, secured to the back of the hand, and a mobile end-effector, placed in contact with the palm. They are connected by two articulated arms, actuated by four servo motors housed on the upper body and along the arms. The end-effector is a foldable flat surface that can make/break contact with the palm to provide pressure feedback, move sideways to provide skin stretch and tangential motion feedback, and fold to elicit the sensation of interacting with different curvatures. The paper presents the design of the wearable haptic device, together with its mobility, statics, and manipulability, as well as direct, inverse, and differential kinematics. We also present a position control scheme for the device, which is then quantitatively evaluated.

1. Introduction

Wearables are attracting great attention in the mechatronics field, as they provide human users with an intuitive, comfortable, and elegant way to interact with nowadays technology. Haptics technology is no exception, with wearable haptics systems being successfully employed in various scenarios [1], including rehabilitation [2, 3, 4], Virtual and Augmented Reality (VR/AR) [5, 6, 7, 8, 9, 10, 11, 12, 13, 14, 15], and robotic teleoperation [16, 5, 17, 18]. Wearable haptic devices have been proposed for different parts of the body, providing kinesthetic [2, 3, 16, 19], pressure [5, 6, 7, 16, 10, 11, 12, 13, 14], skin stretch [8, 9, 17, 10, 13, 15], and vibration [6, 4, 16] stimuli to the fingers [5, 7, 8, 9, 6, 4], palm [10, 11, 12, 13, 14, 15], full hand [2, 3, 16], and forearm [17, 20]. The primary advantage of wearable haptics is of course the reduced form factor and weight compared to grounded solutions, features that open the possibility of more easily engaging in multi-type ubiquitous haptics, i.e., interactions able to elicit different types of haptic sensansations in a lightweight and portable manner [1]. However, it is not particularly common to find wearable devices designed to provide more than one type of haptic sensation, which is mostly due to form factor and weight constraints: providing more stimuli often means including more actuators, which in turn results in bulkier devices. Moreover, most devices are designed for the fingers, while it is less common to find devices designed to be worn elsewhere [1]. This is mostly due to the fact that the fingers are the most sensitive parts of our body as well as the ones most often used for grasping, manipulation, and probing the environment.

We present a wearable haptic device for the palm, shown in

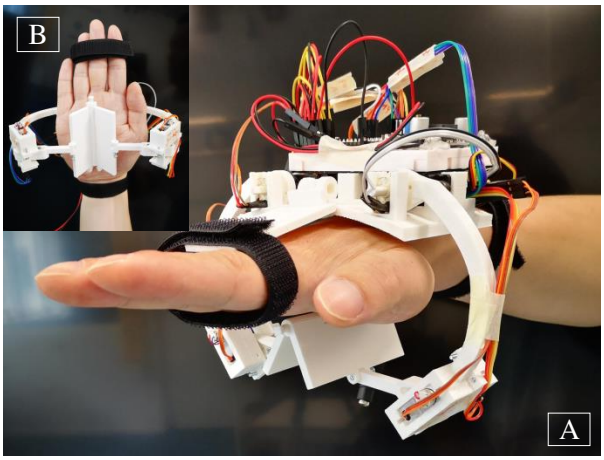

Figure 1: Two views of the proposed 4-DoF wearable haptic device for the palm. The end-effector is composed of two plates connected in a hinge-like structure. Four motors enable the end-effector to move towards/away from the palm, sideways along the hand ulnar-radial direction, and fold in two.

Email addresses: Lisheng.Kuang@irisa.fr (Lisheng Kuang), monica.malvezzi@unisi.it (Monica Malvezzi), marco.ferro@sirisa.fr (Marco Ferro), domenico.prattichizzo@unisi.it (Domenico Prattichizzo), prg@irisa.fr (Paolo Robuffo Giordano), chinello@btech.au.dk (Francesco Chinello), claudio.pacchierotti@irisa.fr (Claudio Pacchierotti)

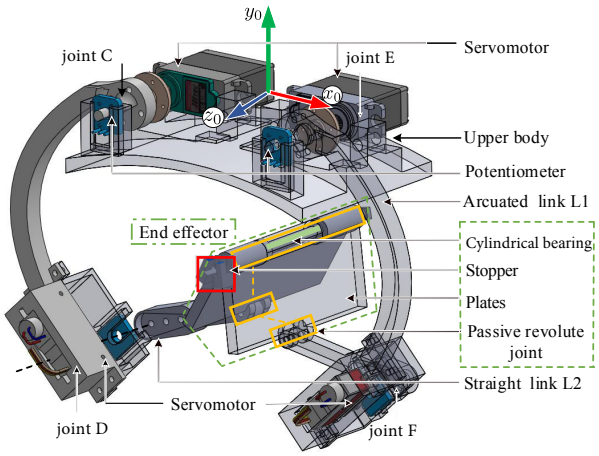

Figure 2: CAD model of the proposed device. It is composed of a static upper body, located on the back of the hand, and a foldable two-piece end-effector placed in contact with the palm. Two articulated arms, composed of arcuated (L1) and straight (L2) sections, connect the two parts. Four servo motors, two on the upper body and two on the arms, actuate the end-effector, enabling it to move along the x_0 and y_0 axes, rotate with respect to z_0 axis, and fold.

Figs. 1 and 2. It features a 4-degrees-of-freedom (4-DoF) end-effector that can move towards/away from the palm, sideways along the hand ulnar-radial direction, and fold in two. The device is therefore able to elicit the sensation of interacting with a wide range of slanted surfaces, curvatures, and even sharp edges through combined localized pressure and skin stretch sensations. Specifically, it can provide localized point (edge) contact with different orientations and edge folding angles, distributed contact over a finite surface, edge sliding over palm surface, and surface sliding over palm surface. The maximum contact force magnitude is configuration-dependent, and can reach 7.33 N.

With respect to other wearable haptic solutions for the palm, such as [10, 11, 12, 13, 14, 15], the proposed device is able to provide a broader range of stimuli, i.e., slanted surfaces, edges, and variable curvature sensations. Moreover, it is accompanied by an in-depth mechanical analysis and evaluation which is missing in the aforementioned works. For example, Minamizawa et al. [10] used two motors to actuate two belts moving a flat end-effector on the palm, providing normal and shear forces. Trinitatova and Tsetserukou [12, 11] used a 3-DoF inverted delta mechanism consisting of three identical kinematic limbs to move a pin-like end-effector across the palm. Similarly, Dragusanu et al. [14] used a 3-DoF parallel tendon-based mechanical structure to actuate an interchangeable palmar end-effector. Guzererler et al. [21] designed a handheld haptic device applying palm skin stretch via an actuated tactor, offering richer feedback than fingertip devices. Their study revealed significant effects of tactor displacement and speed on perceived skin stretch intensity, with non-linear mapping (higher intensity occurs towards the thumb). Provancher and Sylvester [22] studied the impact of fingertip skin stretch on friction perception, aiming to enhance perceived friction in force feedback. Tests revealed that even small fingerpad skin stretches combined with force feedback significantly increased perceived friction, which is really promising for the development of multi-sensory haptic interfaces. Son and Park [23] aimed to enhance cutaneous feedback when interacting with virtual objects by designing a haptic system for the fingers and palm. Their mechanism delivers feedback to the palm alongside the thumb, middle, and index fingers. They demonstrated that integrating cutaneous palm feedback improves perception of large virtual objects compared to relying solely on kinesthetic finger feedback. More recently, Yoshimoto and Yamamoto [24] explored pressure stimuli on the palm, examining their influence on force perception when combined with kinesthetic stimuli. Using the method of adjustment, participants matched pressure to an applied force, revealing significant alterations in force perception due to palm pressure. Cabrera et al. [15, 13] presented a device able to actuate three small contact points using an inverted five-bar linkages. The envisioned application for all these devices is manipulation in VR.

2. Design of the wearable haptic device

The proposed 4-DoF wearable device was designed following the design guidelines for wearable haptics discussed in [1], with the objective of employing it in Virtual Reality and robotic teleoperation applications. The haptic system has been designed to:

1. minimize the impairment for users as well as be as lightweight and comfortable to wear as possible;
2. enable easy mechanical personalization and adaptation for different users [25];
3. render a wide range of haptic stimulation, including making/breaking contact, skin stretch, relative tangential motion, and edges [1].

A prototype of the wearable hand device is shown in Fig. 1, while its CAD design is shown in Fig. 2. Inspired by a dual-arm robot system, the device features a 4-DoF structure with two arms connecting a static upper body to the end-effector, constituting a planar, parallel mechanism. The upper body is fastened to the back of the hand with velcro straps, while the end-effector applies the target haptic stimuli to the user's palm.

Each arm is composed of two rigid serial chains constrained to each other, including an arcuated link (L1 in Fig. 2) and a straight link (L2). Two upper revolute joints C and E connect the arcuated links of each arm to the upper body. Two lower revolute joints D and F connect the arcuated links of each arm to the corresponding straight links L2. The axes of the revolute joints are parallel to each other, making the whole mechanism planar. Finally, each straight link L2 is connected to the end-effector through a passive revolute joint, generating a 2-DoF planar articulated mechanism. The combined action of the two arms leads to the final 4 DoF of the system.

The end-effector is composed of two flat rectangular plates connected in a hinge-like fashion through a passive cylindrical bearing, allowing the folding of the two plates with respect to the z_0 direction (see Fig. 2). Actuated by the combined action of the two arms, the movement of the end-effector is constrained within

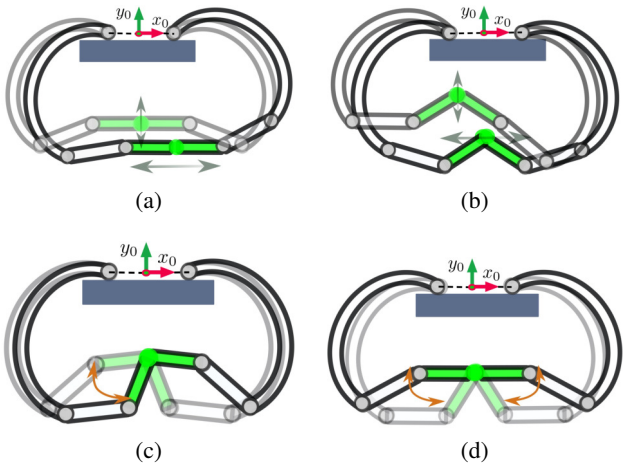

Figure 3: Representative movements of the wearable 4-DoF device. The end-effector, depicted in green, is actuated by the joint action of the arcuated and straight links. (a) Horizontal/vertical movement while the end-effector is fully unfolded, providing variable pressure and skin stretch sensations through a flat surface; (b) Horizontal/vertical movement while the end-effector is partially folded, providing variable pressure and skin stretch sensations through a sharp edge; (c) Roll movement, providing the sensation of interacting with a slanted or uneven surface; (d) Folding/unfolding movement, providing the sensation of interacting with different edges.

the x_0–y_0 plane, referred to as plane Σ, constituted by the joints. In this way, the end-effector can be controlled to move vertically along the y_0 axis, sideways along the x_0 axis, fold, as well as roll. However, since the three joints on the end-effector are passive, we cannot control the direction of the folding, i.e., we cannot control whether the edge created by the folding points upwards or downwards. We included a stopper on the cylindrical bearing between the two plates to constraint the end-effector to fold with the edge pointing upwards, so as to generate the sensation of interacting with edges of different sharpness. Of course, the stopper can be easily adjusted to constraint the end-effector to fold in the other direction.

The electronics system consists of an Atmega328 controller mounted on an Arduino Uno Board. The actuation is provided by two HS-85MG servomotors, mounted on the upper body (in joint C, E), and actuating the arcuated links, and two KST-08H servomotors, mounted on the arms (joint D, F), and actuating the straight links. The torque provided by the servomotors allow the device to apply a force up to 7 N to the palm. The force that can be applied depends on device configuration, as detailed in Sec. 3. We also installed four rotatory Bourns potentiometer 3382H on each servomotor, so as to measure their current shaft rotation angle.

Figure 3 shows a series of representative motions that the device can actuate, while Table 1 summarizes the main characteristics of the device.

Table 1: Device specifications

Weight	160 g
Length × Width × Height	(13–18) × 18 × (12–15) cm
Maximum contact surface	42 cm^2
Control system	Arduino Uno, Atmega328
Communication latency	< 20 ms
Operating voltage range	4.8 to 6.0 V
Operating joints speed	0.14 sec/60°
Maximum normal force	7.33 N
Horizontal displacement	9 cm
Vertical displacement	5 cm

3. Device Analysis

This Section presents the mechanical model of our device, including its mobility analysis as well as the forward and inverse kinematics analysis, necessary to derive the main structural parameters of the device and the kinematic and dynamic modeling.

As shown in Fig. 4, the revolute joints are parallel to each other and aligned in the same plane Σ. Let us indicate with $S_0 < O_0, x_0, y_0, z_0 >$ the reference frame attached to the upper body, in which O_0 is the origin and the center between revolute joints C and E. The x_0 axis is parallel to $\overrightarrow{CE}$, y_0 is in the same plane with x_0, C, and E (plane Σ), and z_0 is consequently defined (see also Fig. 2). The two lower revolute joints on the arcuated links, D and E, are also parallel to the each other and lie in the plane Σ. The two arcuated links L1 have the same structure, their configuration is defined by vectors $\overrightarrow{CD}$ and $\overrightarrow{EF}$, respectively, with length $|\overrightarrow{CD}| = |\overrightarrow{EF}| = l_1$. The straight links L2, connecting the arcuated links to the end-effector, are defined by the vectors $\overrightarrow{DA}$ and $\overrightarrow{FB}$, respectively, with length $|\overrightarrow{DA}| = |\overrightarrow{FB}| = l_2$. Finally, the foldable end-effector is represented by vectors $\overrightarrow{AP}$ and $\overrightarrow{BP}$, with length $|\overrightarrow{AP}| = |\overrightarrow{BP}| = l_3$. The cylindrical bearing between the two plates of the end-effector intersects with the plane Σ at P, where we define the coordinate frame $S_p < O_p, x_p, y_p, z_p >$, with the origin O_p coinciding with P.

3.1. Mobility Analysis

The mobility analysis of our device has similarities with dual arm manipulators and Delta-2 robots, i.e., with both serial and parallel robots. The device is actuated by two serial planar Revolute-Revolute (R-R) chains attached to the upper body, with a foldable two-plates end-effector constraining their movement. These two serial chains manipulate the two plates on the end-effector through passive joints, so as to control its position, orientation, and folding configuration along 4 DoF. A set of representative movements the device can actuate is shown in Fig. 3. Two DoF can be obtained by moving the end-effector within the $x_0 - y_0$ plane (as in Figs. 3a and 3b), one DoF comes when the end-effector rolls with respect to the z_0 direction (as in Fig. 3c), and another DoF lies in the folding movement of the two plates, constrained by the stopper (as in Fig. 3d). These

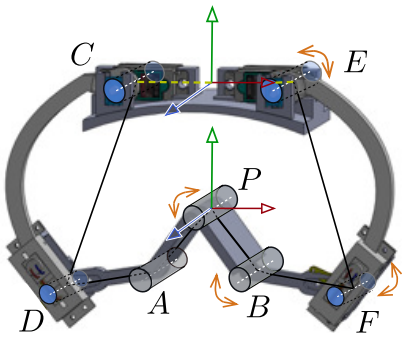

(a)

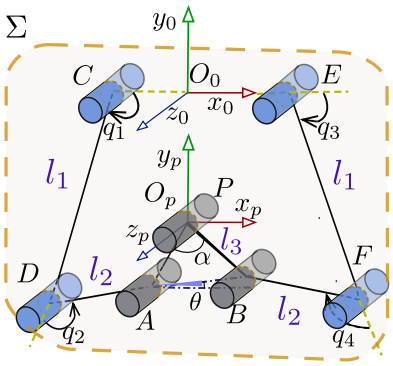

(b)

Figure 4: Kinematic structure of the proposed 4-DoF wearable haptic device. Two planar Revolute-Revolute chains, actuated by four motors, move the end-effector of the device. The position (x_P, y_P) of the middle point of the cylindrical bearing on the end-effector P, the roll angle θ with respect to the $x_0 - z_0$ plane, and the folding angle α define the device active movements.

four DoF can be represented by the four-dimensional vector $\mathbf{u} = [x_P, y_P, \theta, \alpha]^{\mathrm{T}}$, which includes P point coordinates (x_P, y_P) in the $x_0 - y_0$ (Σ) plane, the roll angle θ, and the folding angle α (see Fig. 4).

A physical stopper is placed on the cylindrical hinge to prevent the device from reaching the singular configuration occurring when the faces of the end-effector are parallel to each other. The stopper prevents this occurrence by guaranteeing a maximum angle of P, i.e., 179 degrees in our case.

3.2. Direct kinematics

As shown in Fig. 4, let us indicate with $\mathbf{q} = [q_1, q_2, q_3, q_4]^{\mathrm{T}}$ the input variables, corresponding to the actuators' rotation angles of joints in C, D, E, and F, respectively, and with $\mathbf{u} = [x_P, y_P, \theta, \alpha]^{\mathrm{T}}$ the output control variables (see Sec. 3.1). Direct kinematics analysis aims at defining the relationship mapping $\mathbf{q}$ into $\mathbf{u}$, i.e.,

$$\mathbf{u} = f_d(\mathbf{q}). \tag{1}$$

Given the input variables $\mathbf{q}$, the coordinates $A = (x_A, y_A)$ and $B = (x_B, y_B)$ can be evaluated as in standard planar RR robots, i.e.,

$$x_A = x_C + l_1 \cos(q_1) + l_2 \cos(q_1 + q_2) \tag{2}$$
$$y_A = y_C + l_1 \sin(q_1) + l_2 \sin(q_1 + q_2) \tag{3}$$
$$x_B = x_E + l_1 \cos(q_3) + l_2 \cos(q_3 + q_4) \tag{4}$$
$$y_B = y_E + l_1 \sin(q_3) + l_2 \sin(q_3 + q_4) \tag{5}$$

From these points, it is possible to evaluate angle θ as

$$\theta = \arctan\left(\frac{y_B - y_A}{x_B - x_A}\right), \tag{6}$$

and the distance between A and B as

$$L = \sqrt{(x_B - x_A)^2 + (y_B - y_A)^2}. \tag{7}$$

Since the considered device has a parallel structure, the input variables $\mathbf{q}$ are constrained by the structure. In particular, length L has to satisfy the following inequality:

$$L \leq 2l_3. \tag{8}$$

If this constraint is satisfied, the folding edge angle α can be evaluated as

$$\alpha = 2 \arcsin\left(\frac{L}{2l_3}\right). \tag{9}$$

Finally, P coordinates are given by:

$$x_P = x_A + l_3 \cos(\theta + \pi/2 - \alpha/2) \tag{10}$$
$$y_P = y_A + l_3 \sin(\theta + \pi/2 - \alpha/2) \tag{11}$$

Equations from (2) to (11) constitute the direct kinematics procedure f_d introduced in eq. (1), i.e., the set of operations allowing to evaluate the output variables $\mathbf{u}$ as a function of input variables $\mathbf{q}$.

3.3. Inverse kinematics

In the inverse kinematic problem, the actuator rotation angles $\mathbf{q}$ are evaluated as a function of a set of output variables $\mathbf{u}$, i.e.,

$$\mathbf{u} = f_i(\mathbf{u}) \tag{12}$$

We can start the procedure by evaluating the distance L between A and B as

$$L = 2l_3 \sin\frac{\alpha}{2}. \tag{13}$$

From P coordinates and α and θ angles, A coordinates can be calculated as follows

$$x_A = x_P - l_3 \cos(\theta + \pi/2 - \alpha/2) \tag{14}$$
$$y_A = y_P - l_3 \sin(\theta + \pi/2 - \alpha/2)\,. \tag{15}$$

The B coordinates can be calculated in a similar way. Once A and B point positions are known, the problem can be solved as the inverse kinematics of two standard 2-DoF, R-R planar manipulators; see for instance [26].

3.4. Differential kinematics

In this subsection, we analyse the relationship between joint angular velocities $\dot{\mathbf{q}}$ and output variables velocity $\dot{\mathbf{u}}$. From the kinematic analysis of the mechanism, it results that such a relationship is linear and can be expressed as:

$$\dot{\mathbf{u}} = \mathbf{J}\dot{\mathbf{q}}, \tag{16}$$

where $\mathbf{J}$ is the mechanism Jacobian matrix, i.e., a 4×4 matrix whose elements depend on mechanism configuration $\mathbf{q}$. Following a straightforward kinematics analysis, it is possible to verify that the $\mathbf{J}$ matrix can be evaluated as:

$$\mathbf{J}(\mathbf{q}) = \begin{bmatrix} \mathbf{C} + \mathbf{D}\,[1\ 0]\,\mathbf{B}^{-1}\mathbf{A} \\ [1\ 1]\,\mathbf{B}^{-1}\mathbf{A} \\ [1\ -1]\,\mathbf{B}^{-1}\mathbf{A} \end{bmatrix} \tag{17}$$

with

$$\mathbf{A} = \begin{bmatrix} -y_{AC} & -y_{AD} & y_{BE} & y_{BF} \\ x_{AC} & x_{AD} & -x_{BE} & -x_{BF} \end{bmatrix},$$

$$\mathbf{B} = \begin{bmatrix} y_{PA} & -y_{PB} \\ -x_{PA} & x_{PB} \end{bmatrix},$$

$$\mathbf{C} = \begin{bmatrix} -y_{AC} & -y_{AD} & 0 & 0 \\ x_{AC} & x_{AD} & 0 & 0 \end{bmatrix},$$

$$\mathbf{D} = \begin{bmatrix} -y_{PA} \\ x_{PA} \end{bmatrix};$$

where, for the sake of conciseness, the double-letter subscripts indicate the relative displacement components between two points, e.g., $y_{AC} = y_A - y_C$, $x_{AC} = x_A - x_C$, etc.

Recalling the definition of the output control variables $\mathbf{u}$, output velocities are defined as $\dot{\mathbf{u}} = \left[v_{Px}, v_{Py}, \dot{\theta}, \dot{\alpha}\right]$, i.e., the vector is composed of two linear velocities v_{Px}, v_{Py}, representing P velocity Cartesian components, and two angular velocities. Therefore, the device Jacobian matrix can be divided into two sub-matrices as follows:

$$\mathbf{J}(\mathbf{q}) = \begin{bmatrix} \mathbf{J}_P \\ \mathbf{J}_O \end{bmatrix}, \tag{18}$$

such that

$$\begin{bmatrix} v_{Px} \\ v_{Py} \end{bmatrix} = \mathbf{J}_P\dot{\mathbf{q}}, \quad \begin{bmatrix} \dot{\theta} \\ \dot{\alpha} \end{bmatrix} = \mathbf{J}_O\dot{\mathbf{q}}. \tag{19}$$

3.5. Statics

The transpose of the Jacobian matrix previously evaluated is also useful for the statics analysis of the mechanism. Let us consider a generic configuration defined by joint variables $\mathbf{q}$, and let us assume that, in such configuration, the device is in a static equilibrium condition under the action of an external interaction vector $\mathbf{w}$ and a vector of motor torques $\boldsymbol{\tau}$. The vector of motor torques has the same dimensions of $\mathbf{q}$ and contains the torques applied by each of the device motors $\boldsymbol{\tau} = [\tau_1, \cdots, \tau_4]^{\mathrm{T}}$, while $\mathbf{w}$ is defined on the basis of $\mathbf{u}$ components, as $\mathbf{w} = [f_x, f_y, \tau_\theta, \tau_\alpha]^{\mathrm{T}}$, where f_x, f_y are the components of the interaction force that the environment applies on P, τ_θ is an external torque that corresponds to a rotation θ (as in Fig. 3c), while τ_α is an external torque that corresponds to a rotation α (as in Fig. 3d).

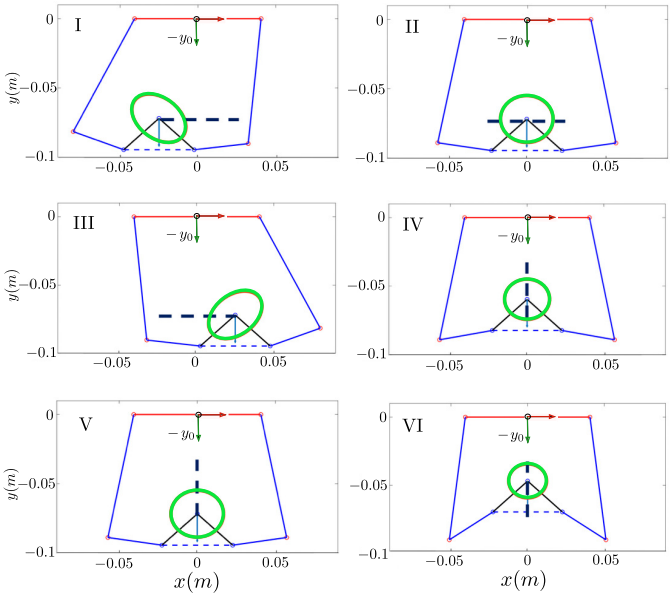

Figure 5: Manipulability analysis. Position kinematic manipulability ellipses for x and y velocity components in six representative device configurations. In each subfigure, a scheme of the device is reported. The red link represent the static upper body, the blue lines represent the links driven by the motors, the black lines represent the passive links on the end-effector, the manipulability ellipse is reported in thick green, centered on the end-effector middle point P. Subplots I-III show a horizontal trajectory (black, thick, dashed line), subplots IV-VI show a vertical trajectory.

In statics equilibrium conditions, by applying the Principle of Virtual Works to the device, it is straightforward to verify that

$$\boldsymbol{\tau} = -\mathbf{J}^{\mathrm{T}}\mathbf{w}. \tag{20}$$

This relationship allows to evaluate the set of motor torques $\boldsymbol{\tau}$ that have to be applied to balance an external interaction vector $\mathbf{w}$.

It is also worth noticing that the relationship between the motor torques $\boldsymbol{\tau}$ and the interaction vector $\mathbf{w}$ depends on $\mathbf{q}$, since the Jacobian matrix $\mathbf{J}^{\mathrm{T}}$ depends on the mechanism configuration.

To estimate the sensitivity of the actuator torques with respect to the mechanism configuration, let us consider an arbitrary reference configuration $\mathbf{q}_0$. In such a configuration, if an external interaction $\mathbf{w}_0$ is applied, the corresponding set of torques required to maintain the mechanism in the equilibrium configuration is $\boldsymbol{\tau}_0 = -\mathbf{J}(\mathbf{q}_0)^{\mathrm{T}}\mathbf{w}_0$. Let us consider an arbitrarily small perturbation with respect to this equilibrium configuration, i.e., $\mathbf{w} = \mathbf{w}_0 + \delta\mathbf{w}$, $\mathbf{q} = \mathbf{q}_0 + \delta\mathbf{q}$, $\boldsymbol{\tau} = \boldsymbol{\tau}_0 + \delta\boldsymbol{\tau}$. If the new configuration is still an equilibrium one, by neglecting higher order infinitesimal terms, it is possible to verify that

$$\delta\boldsymbol{\tau} = -\mathbf{J}(\mathbf{q}_0)^{\mathrm{T}}\delta\mathbf{w} - \left[\frac{\partial(\mathbf{J}(\mathbf{q})^{\mathrm{T}}\mathbf{w}_0)}{\partial\mathbf{q}}\right]\delta\mathbf{q}, \tag{21}$$

where the term

$$\mathbf{K}_q = \left[\frac{\partial(\mathbf{J}(\mathbf{q})^{\mathrm{T}}\mathbf{w}_0)}{\partial\mathbf{q}}\right] \tag{22}$$

allows to estimate the sensitivity of actuators torques with respect to errors or disturbance in the mechanism configuration estimation. This term is useful to understand the impact of the position tracking and position control errors on the actuators torques. Even if $\mathbf{K}_q$ elements are dimensionally a stiffness, these terms do not represent physical stiffness elements, but rather they take into account the dependence of the Jacobian on the configuration. For this reason, they are usually referred to as geometric terms [27]. Furthermore, even if $\mathbf{K}_q$ is square (4×4), it is in general nonsymmetric [28] and depends on $\mathbf{w}_0$. The analytical expression of $\mathbf{K}_q$ has not been reported for the sake of space; its evaluation is available in the MATLAB script included as supplemental material.

3.6. Manipulability

Manipulability analysis is widely adopted in robotics and mechanics to evaluate the effectiveness of a mechanism to transmit velocities and forces [29]. The kinematic manipulability index, in particular, is defined in each configuration as

$$\kappa = \sqrt{\det(\mathbf{J}\mathbf{J}^{\mathrm{T}})}. \tag{23}$$

It is worth noticing that this expression cannot be directly evaluated since the elements of $\mathbf{J}$ are not dimensionally homogeneous. In fact, the elements on the first two rows are lengths (they relate a linear velocity to an angular velocity), while the elements of the last two rows are dimensionless. To avoid this problem, we defined two different manipulability indices (see also eq. 18):

$$\kappa_P = \sqrt{\det(\mathbf{J}_P\mathbf{J}_P{}^{\mathrm{T}})}, \tag{24}$$

$$\kappa_O = \sqrt{\det(\mathbf{J}_O\mathbf{J}_O{}^{\mathrm{T}})}. \tag{25}$$

More in general, in each configuration, manipulability analysis defines how a unit sphere in the joint-velocity space, i.e., $\dot{\mathbf{q}}^{\mathrm{T}}\dot{\mathbf{q}} = 1$, is mapped in the end-effector velocity sphere. Given the linear and configuration-dependent relationship between joints and end-effector velocities $\dot{\mathbf{u}}$ established in eq. (16), it is straightforward to see that the sphere is mapped into an ellipsoid, whose equation is $\dot{\mathbf{u}}^{\mathrm{T}}\mathbf{J}^{-\mathrm{T}}\mathbf{J}^{-1}\dot{\mathbf{u}} = 1$. The semi-axes of such an ellipsoid are oriented as the eigenvectors of the matrix $\mathbf{J}\mathbf{J}^{\mathrm{T}}$; the square-root of its eigenvalues returns, instead, their lengths.

The analysis of the manipulability ellipsoid provides some interesting information on the mechanism properties. In particular, it is clear that, when the mechanism approaches a singular configuration, the ellipsoids volume drops to zero. Furthermore, a sphere-shaped ellipsoid indicates a rather isotropic transmission behavior, i.e., the mechanism can move in any direction with approximately the same joint velocities. On the other side, a flatten ellipsoid indicates that, in such configuration, the mechanism can move more efficiently in the direction corresponding to the larger semi-axes, while moving in the directions corresponding to the smaller semi-axes requires higher joint velocities. In the analysed mechanism, both $\dot{\mathbf{q}}$ and $\dot{\mathbf{u}}$ are $\mathbb{R}^4$ vectors, so the ellipsoid is four-dimensional. Furthermore, the dimensions of $\dot{\mathbf{u}}$ vector elements are not homogeneous, since it contains two linear and two angular velocities. For the sake of clarity, in this analysis we only considered the linear velocities, i.e., we evaluate the two-dimensional projection of the manipulability ellipsoid in the v_{Px}-v_{Py} plane, that is an ellipse.

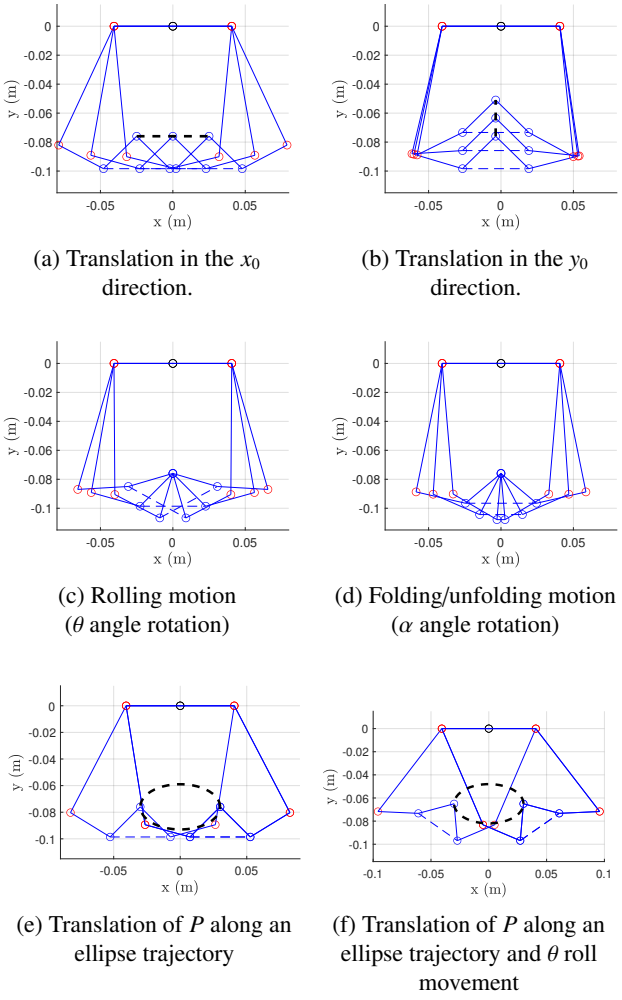

(a) Translation in the x_0 direction.

(b) Translation in the y_0 direction.

(c) Rolling motion (θ angle rotation)

(d) Folding/unfolding motion (α angle rotation)

(e) Translation of P along an ellipse trajectory

(f) Translation of P along an ellipse trajectory and θ roll movement

Figure 6: Numerical simulations: Kinematic scheme of the device in the initial and final configurations of the considered movements. Blue lines represent the mechanism links, black dashed lines represent the trajectory of P.

Fig. 5 shows how the position kinematic manipulability ellipse varies during two representative trajectories. The first three figures (I, II, III) have been realized by moving the end-effector horizontally along a direction parallel to x_0 axis, the second three (IV, V, VI) by moving it vertically along the y_0 axis. The analysis has been carried out on a wider set of configurations, spanning the operative device workspace, verifying that the manipulability index is, in all the analysed cases, sufficiently far from zero and that the device is sufficiently far from singularities. Such results can be verified by running the MATLAB script included as supplemental material.

Manipulability analysis is also useful for carrying out a preliminary evaluation of the force feedback capabilities of the device. In particular, similarly to the kinematic manipulability index, the *force* manipulability index is defined as the ratio of a

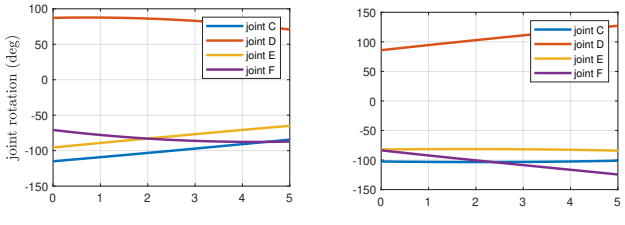

(a) Translation in the x_0 direction.

(b) Translation in the y_0 direction.

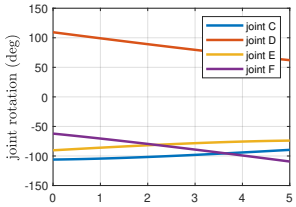

(c) Rolling motion (θ angle rotation)

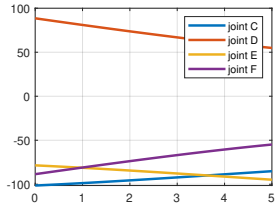

(d) Folding/unfolding motion (α angle rotation)

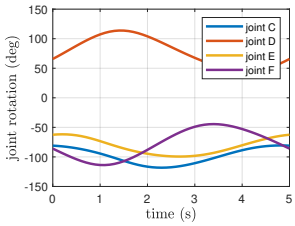

(e) Translation of P along an ellipse trajectory

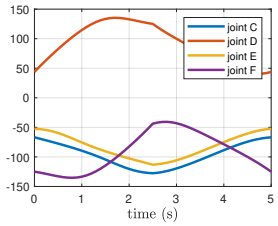

(f) Translation of P along an ellipse trajectory and θ roll movement

Figure 7: Numerical simulations: Rotation angles of actuated joints C, D, E, F as a function of time.

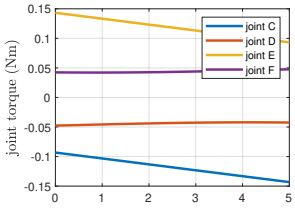

(a) Translation in the x_0 direction.

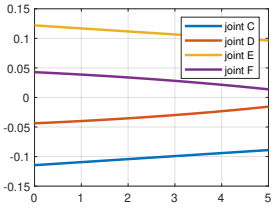

(b) Translation in the y_0 direction.

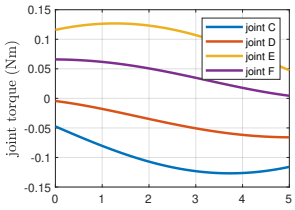

(c) Rolling motion (θ angle rotation)

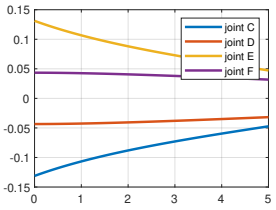

(d) Folding/unfolding motion (α angle rotation)

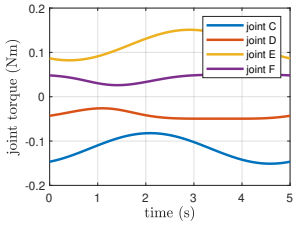

(e) Translation of P along an ellipse trajectory

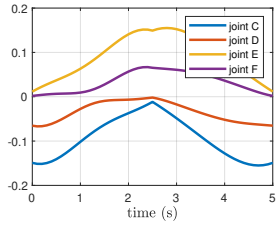

(f) Translation of P along an ellipse trajectory and θ roll movement

Figure 8: Numerical simulations: Joint torques applied by the motors in joints C, D, E, F as a function of time, when a 2 N force is applied on P towards the $-y_0$ direction.

performance measure in the space of forces exchanged with the environment and an effort measure in the space of actuated joint torques, i.e.,

$$\kappa_f = \frac{\delta \mathbf{w}^{\mathrm{T}} \mathbf{W}_w \delta \mathbf{w}}{\delta \boldsymbol{\tau}^{\mathrm{T}} \mathbf{W}_\tau \delta \boldsymbol{\tau}}, \tag{26}$$

where $\mathbf{W}_w$ and $\mathbf{W}_\tau$ are weight matrices that can be defined for properly weighting the different components and for adjusting the dimension units of $\mathbf{w}$ and $\boldsymbol{\tau}$, respectively. By considering eq. (20), it is possible to verify that, also in this case, a unit sphere in the actuator torque space is mapped into an ellipsoid in the end-effector force space. Assuming $\mathbf{W}_w$ and $\mathbf{W}_\tau$ as identity matrices for the sake of simplicity, lengths of the ellipsoid semi-axes can be evaluated as the square-root of the eigenvalues of $\left(\mathbf{J}\mathbf{J}^{\mathrm{T}}\right)^{-1}$, and their

orientations are given by its eigenvectors. It is straightforward to verify that the semiaxes of the kinematic and force manipulability ellipsoids have the same orientation, while the lengths of the first one are the reciprocal of the second one.

3.7. Numerical simulations

Figures 6–10 report the results of a series of numerical simulations. They aim at testing whether the device can operate with suitable manipulability levels during a set of six representative movements for haptic applications.

Subfigures (a) of Figs. 6–10 show a translation of P along the x_0 direction, with a 26 mm stroke. The trajectory is travelled, with constant speed, in 10 s, while θ and α are maintained constant. Subfigures (b) show a translation of P along the y_0 direction, with a 16 mm stroke. Also in this case, the speed is constant and the trajectory is travelled in 10 s, while θ and α are maintained constant. Subfigures (c) show a roll movement in which the θ angle decreases linearly from 15° to 0° in the first 5 s and then increases from 0° to 15° in the remaining 5 s. The α angle and the position of P are maintained constant. Subfigures (d) show a folding/unfolding movement in which the α angle decreases linearly from 110° to 20° in the first 5 s and then increases from 20° to 110° in the remaining 5 s. The θ angle and the position of P position are maintained constant. Subfigures (e) show a translation movement of P that follows an ellipse with semi-axes 30 mm and 17 mm in the x_0 and y_0 directions, respectively, during 10 s. θ and α angles are maintained constant. Finally, subfigures (f) show the same ellipse trajectory travelled by P in 10 s, but this time coupled with a roll movement θ, which varies from $-35°$ to 35°. The α angle is maintained constant.

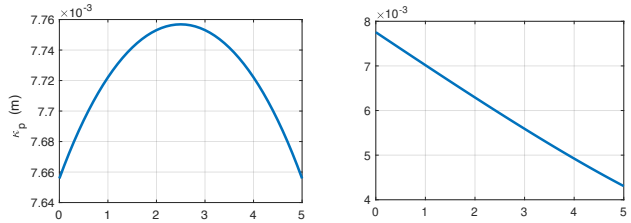

(a) Translation in the x_0 direction.

(b) Translation in the y_0 direction.

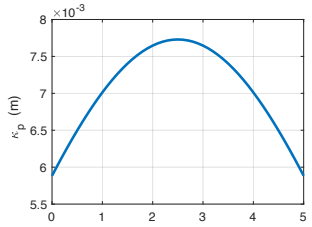

(c) Rolling motion (θ angle rotation)

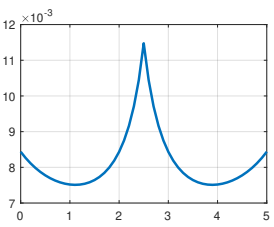

(d) Folding/unfolding motion (α angle rotation)

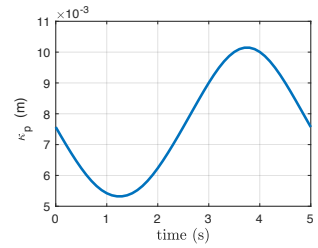

(e) Translation of P along an ellipse trajectory

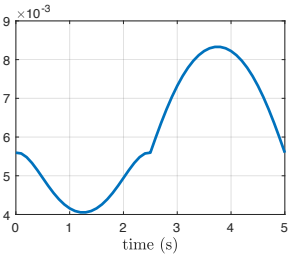

(f) Translation of P along an ellipse trajectory and θ roll movement

Figure 9: Numerical simulations: Kinematic manipulability index κ_p evaluated considering the position Jacobian matrix $\mathbf{J}_p$.

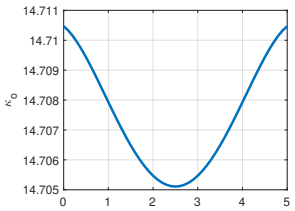

(a) Translation in the x_0 direction.

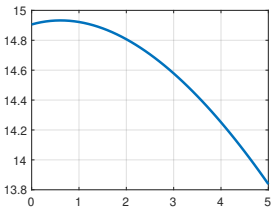

(b) Translation in the y_0 direction.

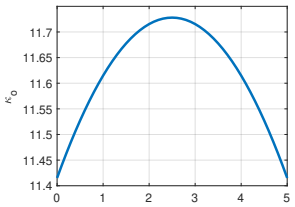

(c) Rolling motion (θ angle rotation)

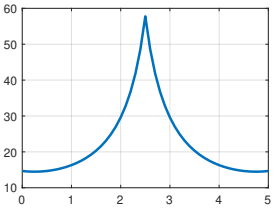

(d) Folding/unfolding motion (α angle rotation)

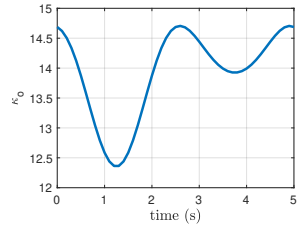

(e) Translation of P along an ellipse trajectory

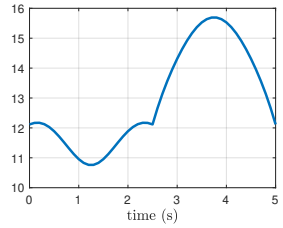

(f) Translation of P along an ellipse trajectory and θ roll movement

Figure 10: Numerical simulations: Kinematic manipulability index κ_o evaluated considering the orientation Jacobian matrix $\mathbf{J}_o$.

Fig. 6 reports the kinematics scheme of the device in the initial and final configurations (blue, thin lines) of the above movements, as well as the trajectory of point P (black, thick dashed line). Fig. 7 shows the rotation angles of the actuated joints C, D, E, F (see Fig. 2). To obtain these angles, we performed the inverse kinematic analysis (see Sec. 3.3), starting from the trajectory defined in the workspace. Fig. 8 shows the joint torques the motors need to apply to resist a representative constant force of 2 N applied on P towards the $-y_0$ direction. Finally, Figs. 9 and 10 show the kinematic manipulability indices κ_P and κ_O, evaluated from eq. (24) and (25). Results relative to force manipulability have not been reported here for the sake of space, however, assuming that the interaction vector contains the interaction force only, i.e., $\mathbf{w} = [f_x, f_y, 0, 0]^{\mathrm{T}}$, the force manipulability index κ_f can be evaluated straightforwardly as $\kappa_f = 1/\kappa_P$. Each subfigure (a)-(f) in Figs. 6–10 refers to one of the six movements described at the beginning of this subsection.

Results show that device workspace is compatible with design requirements for haptic interactions on hand palm. In all the simulated cases, the inverse kinematics procedure provides physically feasible solutions. The torques necessary to resist a force applied on P with magnitude 2N are clearly configuration-dependent, but always compatible with the motor characteristics in all the simulated cases. Manipulability indices κ_P and κ_O vary according to the different simulated configurations, but their values are sufficiently far from zero, reflecting that there are no singularity issues.

The inverse kinematic procedure was also used to identify, for a set of nine representative combinations of angles α and θ, the area in the xy plane that can be reached by point P, to further verify that the device satisfies the design requirements about workspace dimensions summarized in Table 1. Results are reported in Fig. 11. As expected, the set of configurations that can be reached depends on α and θ values. However, in all the nine considered combinations, the maximum horizontal displacement and the maximum vertical displacement are compatible with the specifications in Table 1.

An additional numerical evaluation was performed to analyze the behavior of the device in terms of force transmission capabilities, in particular in configurations close to singularities. Specifically, considering the configuration in which the end-effector is close to being completely unfolded, the maximum normal force that can be controlled decreases. Considering the maximum torque that can be applied by the servomotors currently employed in the device, the maximum force that can be applied as a function of the angle α is reported in Fig. 12: it

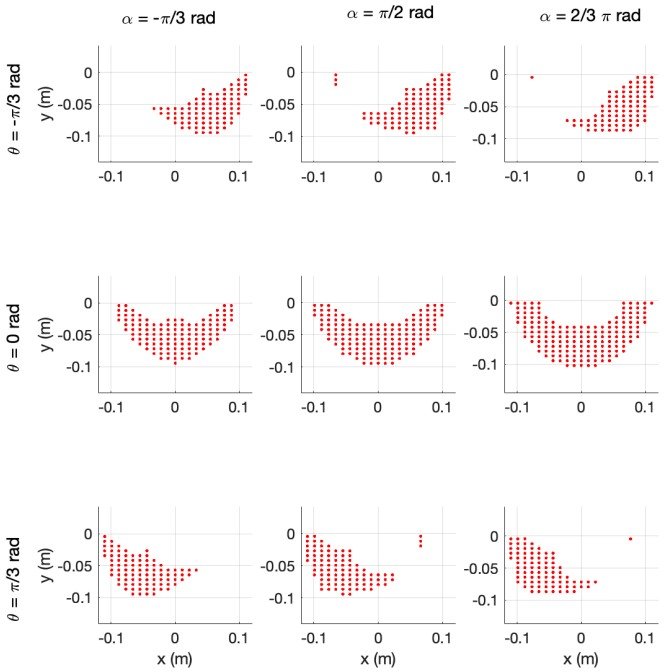

Figure 11: Numerical simulations: workspace evaluation. Dotted areas in the diagrams represent P point positions that can be reached for three different values of θ ($\theta = [-\pi/3, 0, \pi/3]$ rad, represented by rows) and α ($\theta = [\pi/3, \pi/2, 2/3\pi]$ rad, represented by columns).

can be noticed that, when the edge is almost flat, the maximum vertical force that can be controlled drops to 0.1 N.

A wider set of simulations can be carried out using the MATLAB script included as supplemental material (see also Sec. 3.8).

3.8. CoppeliaSim kinematic model

We also present a simulated model of the device, which replicates its kinematic structure and mechanics as described in the previous Sections. Each link of the kinematic chain is realized through the composition of three objects: i) the virtual joint that is responsible of the link motion, ii) a simple cuboid shape defining the kinematic connection between the same joint and the subsequent one along the chain, iii) a visual mesh extracted from the device CAD model, with the same structure of the corresponding link of the real device. Each joint is commanded through position inputs: in particular, given an arbitrary configuration of the two serial arms, specified through the vector $\mathbf{q}$ of the active joints C, D, E and F, the closed-chain structure is guaranteed by forcing the position of the passive joints A and P as

$$\begin{aligned} q_A &= \theta + (\pi - \alpha)/2 - q_1 - q_2 \\ q_P &= q_A + \alpha. \end{aligned} \tag{27}$$

The CoppeliaSim scene containing this model, along with a MATLAB script computing the appropriate joint configuration vector $\mathbf{q}$ for a set of representative trajectories (see also Sec. 5.3), are available as supplemental material.

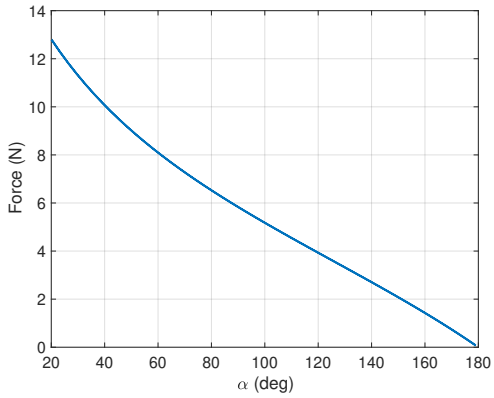

Figure 12: Numerical simulations: maximum normal force that can be applied to the palm for different values of the folding angle α, considering $\theta = 0$, $x_P = 0$, $y_P = -0.079$ m.

4. Control Implementation

According to the device mechanism and type of interaction to be rendered, our device can be controlled in different ways. We present here a position control scheme, along with its evaluation.

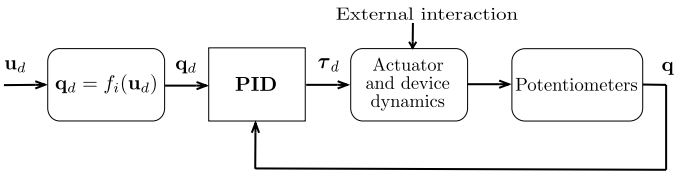

Figure 13: Position control system. The reference configuration is provided in the end-effector configuration space $\mathbf{u_d}$. The inverse kinematics procedure described in Sec. 3 allows to convert the desired configuration in the joint space. Finally, a PID controller is implemented, providing the desired motor torque $\boldsymbol{\tau}_d$. The actual joint configuration is measured by the potentiometers placed on the device active joints (C, D, E, F – see Fig. 2).

4.1. Device position control

The device position control focuses on controlling the position and orientation of the end-effector. This can be implemented in two ways. The first is to manipulate the end-effector as a rigid fixed-shaped object: in this case, its orientation and folding angle are kept constant, while its position with respect to the upper body coordinate $S_0 < x_0, y_0, z_0 >$ is modified by the two articulated arms. The second is to manipulate the end-effector as a flexible coupling hinge by rotating the two plates composing the end-effector: in this case, its position with respect to the upper body coordinate $S_0 < x_0, y_0, z_0 >$ is kept constant, while the orientation of the end-effector and the angle between its two plates varies. By combining these two levels, the two arms can move and orient the end-effector within its allowed workspace. Both the levels can be schematised and managed as shown in Fig. 13, where the task can be defined in the end-effector configuration space as a sequence of desired configurations $\mathbf{u}_d$. The

inverse kinematics procedure detailed in Sec. 3 allows to pass from the end-effector space to the joint space, i.e.,

$$\mathbf{q}_d = f_i(\mathbf{u}_d) \tag{28}$$

The position control is therefore managed at the joint level by means of a PID controller, in which the actual joint configuration $\mathbf{q}$ is provided by the potentiometers.

4.2. Control Evaluation

To evaluate the performance of each actuated joint (C, D, E, F), we commanded step and sinusoidal inputs and analyzed the actual actuated movement. Each actuated joint was tested separately, with the other joints free to move. Each movement was repeated 10 times and their results were averaged.

We considered three step reference inputs, with target amplitudes of 20°, 40°, and 60°, all of which starting from 0°. The rise time is defined as the time required for the signal, i.e., the actual rotation of the joint, to rise from 10 to 90% of its steady value. Fig. 14 and Tab. 2 present the results, showing very little overshooting, a maximum rise time of 0.17 s (on joint E), and a maximum error at steady state of 1.0% (on joint F).

We considered three sinusoidal reference inputs, $r(t) = A\sin(0.4\pi t)$ with amplitudes A = 10°, 20°, and 30°. Fig. 15 present the results. The worst performance was registered on joint D when actuating the sinusoid with A =30°, showing an average tracking error of 6.7% of the amplitude; while the best performance was registered on joints C when actuating the sinusoid with A =10°, showing an average tracking error of 5.1% of the amplitude.

5. Device Performance Evaluation

We evaluate the performance of the proposed device in actuating a set of representative movements.

5.1. Target movements for the end-effector

We considered five representative patterns of motions for the end-effector (see Figs. 3 and 4 for reference):

- M1. a horizontal movement of the end-effector while it is partially folded: P moves of 26 mm along x_0, with α = 100° (see https://youtu.be/ZuB_JxwbB9s?t=20);
- M2. a vertical movement of the end-effector while it is partially folded: P moves of 16 mm along y_0, with α = 100° (see https://youtu.be/ZuB_JxwbB9s?t=44);
- M3. a roll movement of the end-effector while it is partially folded: P is stationary, while θ rolls in [0, 15]° (see https://youtu.be/ZuB_JxwbB9s?t=69);
- M4. a folding/unfolding movement of the end-effector: P is stationary, while α changes in [20, 110]° (see https://youtu.be/ZuB_JxwbB9s?t=94);
- M5. a combined planar/roll movement of the end-effector while it is partially folded: P moves along an ellipse with axes 34 mm and 60 mm (combination of M1 and M2), while θ rotates in [0, 35]° (similar to M3) and α is stationary at 100° (see https://youtu.be/ZuB_JxwbB9s?t=121).

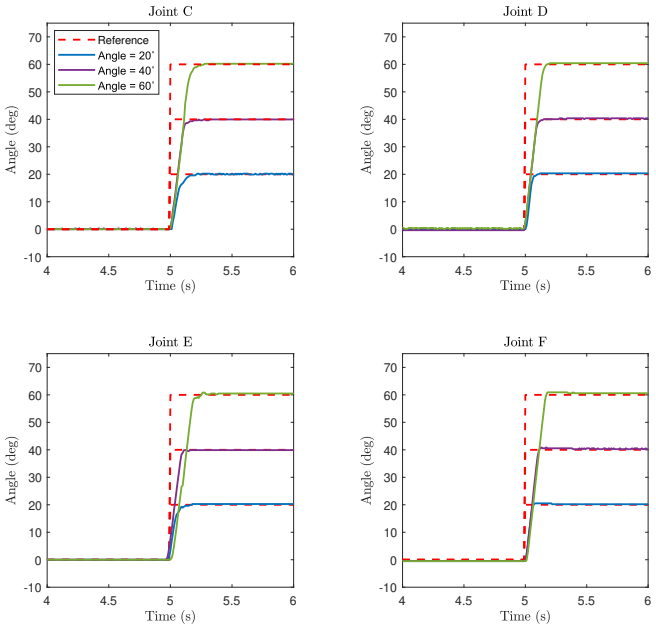

Figure 14: Step response. We commanded the four actuated joints to follow a step command, rotating from 0°to 20°, 40°, or 60°.

Table 2: Step response. Rise time and tracking errors.

	Angle	joint C	joint D	joint E	joint F
Rise time (s)	20°	0.08	0.06	0.07	0.06
	40°	0.14	0.09	0.09	0.11
	60°	0.16	0.15	0.17	0.16
Error (deg)	20°	0.229	0.341	0.273	0.193
	40°	0.270	0.377	0.118	0.558
	60°	0.216	0.429	0.497	0.595

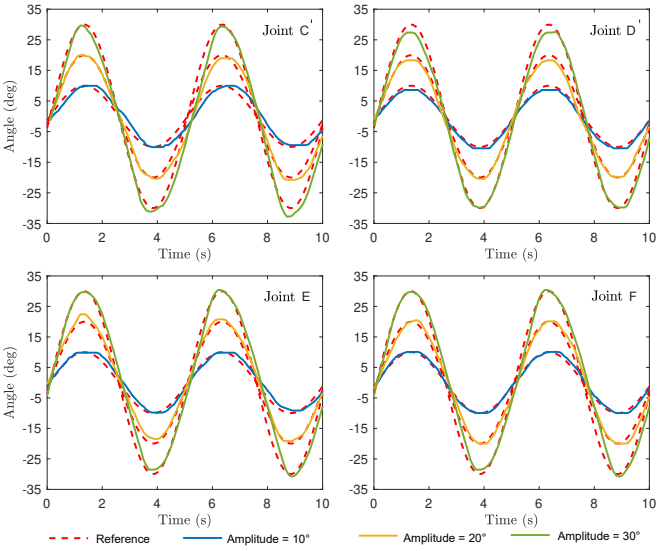

Figure 15: Sine response in tracking response of the four active joints. Sinusoidal inputs with different amplitudes (10°, 20°and 30°).

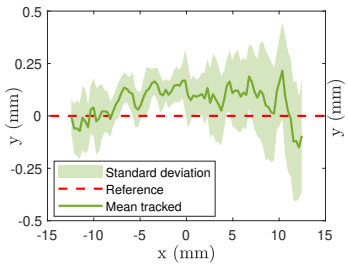

Figure 16: M1: horizontal mov. of P, $x_P \in$[-13, 13] mm.

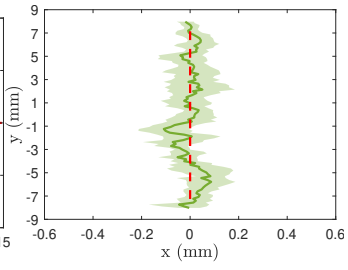

Figure 17: M2: vertical mov. of P, $y_P \in$[-8, 8] mm.

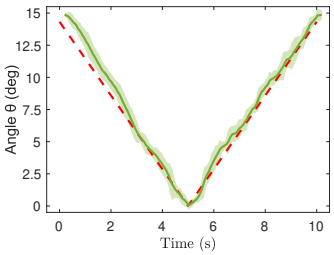

Figure 18: M3: roll movement of $\theta \in [0,15]°$.

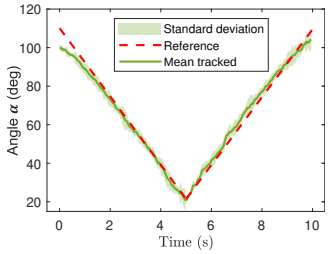

Figure 19: M4: folding movement of $\alpha \in [20,110]°$.

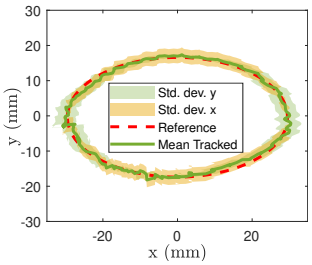

(a) elliptical movement of P, with $x_P \in$[-30, 30] mm and $y_P \in$[-17, 17] mm

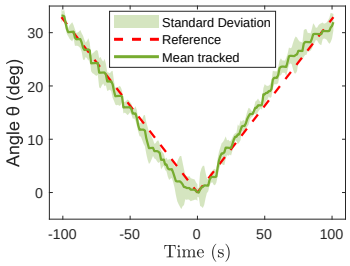

(b) roll movement of $\theta \in [0,35]°$

Figure 20: M5: combined ellipse and roll movement.

These are the same movements also considered in the numerical simulations of Sec. 3.7.

5.2. *Tracking of the end-effector*

To evaluate the error in tracking the target set of movements, we measured the pose of the end-effector using the external optical tracking system OptiTrack (NaturalPoint Corp). It is composed of six infrared cameras (Optitrack Flex-3) sampling the position of six passive markers installed over the two moving plates of the end-effector. The tracking system is connected to a desktop computer (Alienware AURORA R8, Intel Core i7, 16 GB RAM, NVIDIA GeForce 1080), which enable to record the position of the markers and reconstruct the pose and configuration of the end-effector at 100 Hz.

5.3. *Results*

We compared the five target patterns of motion, described in Sec. 5.1 and implemented using the position control of Sec. 4, with the actuated motions, registered using the optical tracking system described in Sec. 5.2.

Table 3: Results of the device performance evaluation.

Pattern (Sec. 5.1)	Error (mean)
M1 (horizontal)	P along x: 1.678 mm (5.60% wrt reference) P along y: 0.057 mm (the smaller the better)
M2 (vertical)	P along x: 0.056 mm (the smaller the better) P along y: 1.537 mm (4.90% wrt reference)
M3 (roll)	θ: 0.686° (4.57% wrt reference)
M4 (folding)	α: 2.305° (2.71% wrt reference)
M5 (ellipse + roll)	P along x: 2.538 mm (4.23% wrt reference) P along y: 1.793 (5.26% wrt reference) θ: 1.323° (3.34% wrt reference)

Figures 16, 17, 18, 19, and 20 report the commanded and tracked mean movements for motions M1, M2, M3, M4, and M5, respectively. Each movement was repeated ten times. Table 3 reports the registered errors, computed as the mean difference between the commanded and tracked motions.

6. Human subjects evaluation

We carried out a human subjects study to test the device capabilities of delivering haptic sensations. Twelve participants (10 males, 2 females, age 22-32, all right-handed) were enrolled in the study. None of the participants reported any visual or haptic perception deficiencies. The experimenter explained the procedures and spent about three minutes adjusting the setup to be comfortable before the subject began the experiment. Due to the different dimension of the hands, for each participant, the device is calibrated to define the make/break contact configuration.

Users were asked to wear the device and recognize a series of haptic patterns, spanning the full rendering space of the device along the four controlled variables of the end-effector, i.e., x_P, y_P, θ and α (see Sec. 4). As detailed in Table 4, for the four variables, we rendered twelve different configurations of the device, considering three variations of each parameter: variations of x_p provided sharp contacts at different points on the palm (see Fig. 21a), variations of y_p provided contacts with different applied forces (see Fig. 21b), variations of θ provides contacts at different orientations (see Fig. 21c), and variations of α provides contact at different sharpness levels (see Fig. 21d). For each configuration, the device end-effector moves towards the user's palm, stays in contact for 2 s, and then breaks contact and moves away. After each interaction, participants are asked to describe what they felt, identifying which sensation/configuration was just provided to them among the different choices reported in Table 4. To avoid order effects, the interactions where randomized using a Latin square design, dividing the interactions in four blocks (one per control variable).

Table 4: Device configurations rendered during the human subjects evaluation, spanning the full rendering space along the 4 controlled parameters. y_0 represents the standard vertical height of the end-effector, calibrated for each subject to ensure good contact.

Ctrl. var.	Considered set	Rendered configuration
x_P	$x_{P,i} \in \{-0.15, 0.0, 0.15\}$ [m]	$\mathbf{u}_d = (x_{P,i}, y_0, 0, \pi/2)^T$
y_P	$y_{P,i} \in \{0.01, 0.02, 0.03\}$ [m]	$\mathbf{u}_d = (0.0, y_0 + y_{P,i}, 0, \pi)^T$
θ	$\theta_i \in \{0.0, \pi/12, \pi/6\}$ [rad]	$\mathbf{u}_d = (0.0, y_0, \theta_i, \pi)^T$
α	$\alpha_i \in \left\{\pi/6, \pi/3, \frac{2}{3}\pi\right\}$ [rad]	$\mathbf{u}_d = (0.0, y_0, 0, \alpha_i)^T$

Results showed an overall recognition rate of 68.75%, with specific rates of 83.3%, 50%, 75% and 66.7% for the sets of control variables x_P, y_P, θ and α, respectively, which is well above the chance level.

The combination of these main "base" renderings can be used to render the sensation of interacting with complex virtual or remote objects. An example of such use has been demonstrated in [30], in which we use these combined renderings to provide feedback in a VR scenario (see the following Section for more details).

7. Discussion and Conclusions

This paper presented a 4-DoF wearable haptic device for the palm. The end-effector is a foldable two-pieces flat surface that can make/break contact with the palm to provide variable pressure stimuli, move sideways to provide skin stretch and tangential motion stimuli, as well as fold to elicit the sensation of interacting with edges of varied nature. With respect to other wearable interfaces for the palm, the proposed device is able to provide a wider range of haptic stimuli, including the rendering of edge sensations, which is rather innovative. It weighs 310 g and features an adjustable structure to adapt to different hand types and sizes. Together with the design of the device, we present its mobility, statics, and manipulability analyses as well as direct, inverse, and differential kinematics, which are in turn used to implement a position control algorithm. The simulated model of the device, both for MATLAB and CoppeliaSim, is available as supplemental material, enabling the reader to further study its structure and rendering capabilities.

Results of our device performance evaluation show that the device is well capable of actuating a wide range of patterns of motion with reduced error and good repeatability. The registered *maximum* error across the considered movements is 2.538 mm (4.23% wrt reference) for displacements and 0.686° (4.57% wrt reference) for rotations. A human subjects study also showed that users are well capable of understanding and recognizing the provided sensations, especially when rendering slanted surfaces and curvatures. On the other hand, vertical movements, i.e., moving the end-effector towards/away from the palm, were found harder to recognize (but still well above the chance level). This latter result can be explained by the fact that, in such interactions, the control of the *force* applied to the palm is more important than the displacement. Future work will address the force control and characterization of the device.

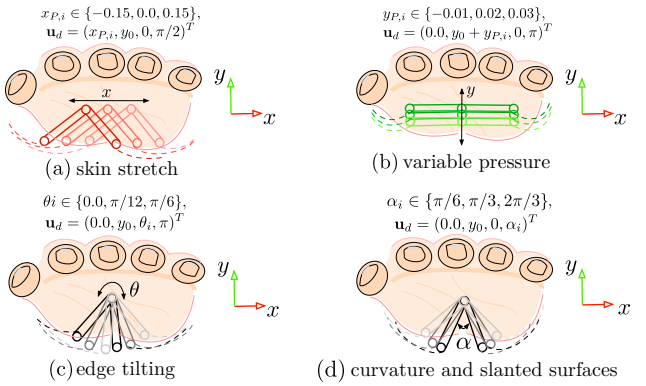

Figure 21: Human subjects evaluation. The device applied a series of haptic patterns (a, b, c, d, in figure) spanning the full rendering space of the device along the four controlled variables of the end-effector: three movements per variable, changing (a) x_p, (b) y_p, (c) θ, and (d) α. Subjects had to recognize which haptic stimulation it was provided.

We envision the use of this device for applications of Virtual Reality (VR) and robotic teleoperation, which have been proven to significantly benefit from cutaneous haptics [31, 32]. In this respect, we have carried out a series of experiments using a similar hand device in immersive VR [30], so as to preliminary show the interface potential in providing complex tactile stimuli. The device has been adapted to support other end-effectors in addition to the one presented in this paper, to simulate the sensation of touching surfaces having different curvatures, stiffness, local shape, and texture. Twelve participants were asked to wear the device and interact with a series of objects in VR, evaluating the immersiveness of the interaction and the realism of the rendering. Subjects results show a rather good performance of the device, e.g., perceived contact realism (ranked 8.4 out of 10) for the hinge-like end-effector (the one presented here) when interacting with rigid objects with different edges, proving the viability of the proposed device for VR applications. The "base" renderings evaluated in Sec. 6 and shown in Fig. 21 are the building blocks for creating these more complex interactions.

The proposed prototype presents also some limitations, mainly due to the use of ABS (hard plastic) and Fused Deposition Modeling, FDM technology for the mechanical structure, which has caused a bit of backslash in the joints. Further optimizations in terms of mechanical structure, materials and manufacturing technologies will lead to better performance in terms of precision, repeatability, and resistance to external loads due to the interaction with the palm or the surrounding environment. Another limitation is due to the geometrical characterisation of the device links, since the device has a planar structure, it can only apply stimuli that do not vary along the hand ulnar-radial direction. One possible solutions could be related to adding a third arm (actuated by two servo motors) between the middle and ring fingers, and changing the constraints, would enable a significantly larger set of motions in 3D space, but increasing the overall structural complexity and wearability. The use of DC motors would also enable better control of the motors torque imparted, beneficial for haptics applications.

A more complete reproduction of an edge with an arbitrary 3D orientation presents a significantly higher complexity, requiring at least 7 DoFs. Similarly, the shape of the end-effector itself limits the type of sensations we can provide, e.g., the edge will always feel like a long thin cylinder. Being able to change the end-effector (as in [30]) and adding additional DoF will enable to significantly extend the rendering capabilities of this device. Such extensions will be the focus of future developments. We also want to carry further human subjects experiments, involving more subjects in a wide range of virtual reality (e.g., immersive interaction with virtual and augmented objects) and robotic teleoperation (e.g., robot-assisted medical palpation, grasping) scenarios.

References

[1] C. Pacchierotti, S. Sinclair, M. Solazzi, A. Frisoli, V. Hayward, D. Prattichizzo, Wearable haptic systems for the fingertip and the hand: taxonomy, review, and perspectives, IEEE Transactions on Haptics 10 (4) (2017) 580–600.

[2] D. Leonardis, M. Barsotti, C. Loconsole, M. Solazzi, M. Troncossi, C. Mazzotti, V. Parenti Castelli, C. Procopio, G. Lamola, C. Chisari, et al., An EMG-controlled robotic hand exoskeleton for bilateral rehabilitation, IEEE Transactions on Haptics (2015).

[3] C. J. Nycz, T. Bützer, O. Lambercy, J. Arata, G. S. Fischer, R. Gassert, Design and characterization of a lightweight and fully portable remote actuation system for use with a hand exoskeleton, IEEE Robotics and Automation Letters 1 (2) (2016) 976–983.

[4] S. Pabon, E. Sotgiu, R. Leonardi, C. Brancolini, O. Portillo-Rodriguez, A. Frisoli, M. Bergamasco, A data-glove with vibro-tactile stimulators for virtual social interaction and rehabilitation, in: Proc. Annual Int. Workshop on Presence, 2007.

[5] I. Sarakoglou, N. G. Tsagarakis, D. G. Caldwell, A compact tactile display suitable for integration in VR and teleoperation, in: Proc. IEEE International Conference on Robotics and Automation (ICRA), 2012, pp. 1018–1024.

[6] M. Gabardi, M. Solazzi, D. Leonardis, A. Frisoli, A new wearable fingertip haptic interface for the rendering of virtual shapes and surface features, in: Proc. IEEE Haptics Symposium, 2016, pp. 140–146.

[7] F. Chinello, C. Pacchierotti, M. Malvezzi, D. Prattichizzo, A three revolute-revolute-spherical wearable fingertip cutaneous device for stiffness rendering, IEEE Transactions on Haptics 11 (1) (2017) 39–50.

[8] C. Pacchierotti, G. Salvietti, I. Hussain, L. Meli, D. Prattichizzo, The hRing: a wearable haptic device to avoid occlusions in hand tracking, in: Proc. IEEE Haptics Symposium, 2016.

[9] A. Girard, M. Marchal, F. Gosselin, A. Chabrier, F. Louveau, A. Lécuyer, Haptip: Displaying haptic shear forces at the fingertips for multi-finger interaction in virtual environments, Frontiers in ICT 3 (2016) 6.

[10] K. Minamizawa, S. Kamuro, N. Kawakami, S. Tachi, A palm-worn haptic display for bimanual operations in virtual environments, in: Proc. Intl. Conf. Human Haptic Sensing and Touch Enabled Computer Applications, 2008, pp. 458–463.

[11] D. Trinitatova, D. Tsetserukou, Touchvr: A wearable haptic interface for vr aimed at delivering multi-modal stimuli at the user's palm, in: Proc, SIGGRAPH Asia XR, 2019, pp. 42–43.

[12] D. Trinitatova, D. Tsetserukou, Deltatouch: a 3d haptic display for delivering multimodal tactile stimuli at the palm, in: Proc. IEEE World Haptics Conference (WHC), 2019, pp. 73–78.

[13] M. Altamirano Cabrera, D. Tsetserukou, Linkglide: a wearable haptic display with inverted five-bar linkages for delivering multi-contact and multi-modal tactile stimuli, in: Proc. International AsiaHaptics Conference, 2018, pp. 149–154.

[14] M. Dragusanu, A. Villani, D. Prattichizzo, M. Malvezzi, Design of a wearable haptic device for hand palm cutaneous feedback, Frontiers in Robotics and AI (2021) 254.

[15] M. A. Cabrera, J. Tirado, J. Heredia, D. Tsetserukou, Linkglide-s: A wearable multi-contact tactile display aimed at rendering object softness at the palm with impedance control in vr and telemanipulation, arXiv preprint arXiv:2208.14149 (2022).

[16] R. M. Khurshid, N. Fitter, E. Fedalei, K. Kuchenbecker, Effects of grip-force, contact, and acceleration feedback on a teleoperated pick-and-place task, IEEE Transactions on Haptics (May 2016).

[17] F. Chinello, C. Pacchierotti, J. Bimbo, N. G. Tsagarakis, D. Prattichizzo, Design and evaluation of a wearable skin stretch device for haptic guidance, IEEE Robotics and Automation Letters 3 (1) (2017) 524–531.

[18] Y. Lee, M. Kim, Y. Lee, J. Kwon, Y.-L. Park, D. Lee, Wearable finger tracking and cutaneous haptic interface with soft sensors for multi-fingered virtual manipulation, IEEE/ASME Transactions on Mechatronics 24 (1) (2018) 67–77.

[19] B. Lim, C. Lee, D. Hwang, Development of embedded sensor system for 5-dof finger-wearable tactile interface, IEEE/ASME Transactions on Mechatronics 26 (4) (2021) 1728–1736.

[20] T. K. Moriyama, A. Nishi, R. Sakuragi, T. Nakamura, H. Kajimoto, Development of a wearable haptic device that presents haptics sensation of the finger pad to the forearm, in: Proc. IEEE Haptics Symposium (HAPTICS), 2018, pp. 180–185.

[21] A. Guzererler, W. R. Provancher, C. Basdogan, Perception of skin stretch applied to palm: Effects of speed and displacement, in: Haptics: Perception, Devices, Control, and Applications: 10th International Conference, EuroHaptics 2016, London, UK, July 4-7, 2016, Proceedings, Part I 10, 2016, pp. 180–189.

[22] W. R. Provancher, N. D. Sylvester, Fingerpad skin stretch increases the perception of virtual friction, IEEE Transactions on Haptics 2 (4) (2009) 212–223.

[23] B. Son, J. Park, Haptic feedback to the palm and fingers for improved tactile perception of large objects, in: Proc. ACM Symposium on User Interface Software and Technology, 2018, pp. 757–763.

[24] S. Yoshimoto, A. Yamamoto, Pressure stimulus to the palm substitutes and augments force sensation, IEEE Transactions on Haptics 14 (4) (2021) 930–935.

[25] M. Malvezzi, F. Chinello, D. Prattichizzo, C. Pacchierotti, Design of personalized wearable haptic interfaces to account for fingertip size and shape, IEEE Transactions on Haptics 14 (2) (2021) 266–272.

[26] L. Sciavicco, B. Siciliano, Modelling and control of robot manipulators, Springer Science & Business Media, 2001.

[27] S.-F. Chen, I. Kao, Conservative congruence transformation for joint and cartesian stiffness matrices of robotic hands and fingers, The International Journal of Robotics Research 19 (9) (2000) 835–847.

[28] N. Ciblak, H. Lipkin, Asymmetric cartesian stiffness for the modelling of compliant robotic systems, in: International Design Engineering Technical Conferences and Computers and Information in Engineering Conference, Vol. 12860, American Society of Mechanical Engineers, 1994, pp. 197–204.

[29] J. P. Merlet, Jacobian, Manipulability, Condition Number, and Accuracy of Parallel Robots, Journal of Mechanical Design 128 (1) (2005) 199–206.

[30] L. Kuang, M. Malvezzi, M. Ferro, D. Prattichizzo, F. C. Paolo Robuffo Giordano, C. Pacchierotti, A wearable haptic device for virtual reality with multiple end-effectors, IEEE Trans. Haptics (2023).

[31] M. Marchal, C. Pacchierotti, Virtual reality and haptics, in: B. Siciliano (Ed.), Robotics Goes MOOC, Springer Cham, 2023.

[32] C. Pacchierotti, D. Prattichizzo, Cutaneous/tactile haptic feedback in robotic teleoperation: Motivation, survey, and perspectives, IEEE Transactions on Robotics (2024).

Lisheng Kuang is a PhD candidate at CNRS-IRISA in Rennes, France. He got a master degree of control engineering from Harbin Institute of Technology (Shenzhen), in 2017. He was a research associate at the Italian Institute of Technology, Genova, Italy in 2019. He visited the Extended Reality and Robotics (xR²) Lab at Aarhus University in 2022. His research focuses on the design, prototyping, testing, and control of wearable robots for applications in human mobility aids.

Monica Malvezzi is an Associate Professor at the University of Siena and Visiting Scientist at the Istituto Italiano di Tecnologia in Genova. She earned her Ph.D. degree in applied mechanics from the Univ. Bologna in 2003. She has also been Researcher at the University of Florence from 2002 to 2008. Her main research interests include control of mechanical and mechatronic systems, robotics, haptics, vehicle localization, multibody dynamics, grasping, and dexterous manipulation.

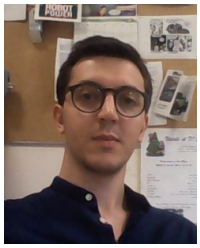

Marco Ferro is a postdoc at CNRS-IRISA in Rennes, France, since 2022. He was previously postdoc at the Department of Computer, Control, and Management Engineering (DIAG) of Sapienza University of Rome, Italy, where he got also his Ph.D. in 2019. He visited the LIRMM in Montpellier in 2014 as intern, and he was a visting Ph.D student at CNRS-IRISA in Rennes in 2018. He worked on vision-based control and estimation methods for humanoid and surgical robots, focusing on the scientific and technological problems in the medical robotics domain.

Paolo Robuffo Giordano received his MSc in Computer Science Engineering in 2001, and his PhD in Systems Engineering in 2008, both from the University of Rome "La Sapienza". In 2007 and 2008 he spent one year as a Postdoc at the Institute of Robotics and Mechatronics of the German Aerospace Center (DLR), and from 2008 to 2012 he was Senior Research Scientist at the Max Planck Institute for Biological Cybernetics in Tübingen, Germany. He is currently a senior CNRS researcher head of the Rainbow group at IRISA and Inria in Rennes, France. He received the 2018 IEEE Robotics and Automation Letters best paper award, and he is Editor of the IEEE Transactions on Robotics.

Francesco Chinello is an Associate Professor of the Department of Business Development and Technology at the Aarhus University, Denmark. He earned his Ph.D. degree in Automatic Control and Robotics from the University of Siena in 2014. Chinello was previously a postdoctoral researcher at University of Siena and fellow at the Italian Institute of Technology, from 2014 to 2016. He also visited the Neural Control of Movement Laboratory of the Arizona University in 2013 and 2014. His research interests include robotics, control, design of haptic interfaces, human-robot interaction, and human-human interaction through wearable devices.

Domenico Prattichizzo is Full Professor of Robotics at the University of Siena, Senior Scientist at the Istituto Italiano di Tecnologia in Genova, and co-founder of WEART. He received the Ph.D. degree in robotics and automation from the University of Pisa in 1995. In 1994, he was a Visiting Scientist with the MIT AI Laboratory. He received the IEEE 2009 Chapter of the Year Award. He served as the Vice-Chair for Special Issues of the IEEE Technical Committee on Haptics and the Chair of the Italian Chapter from the IEEE RAS, from 2006 to 2010. He also served as the Chair for the IEEE RAS Early Career Awards Evaluation Panel in 2013. He serves as the Editor-in-Chief for the IEEE Transactions on Haptics.

Claudio Pacchierotti is a tenured researcher at CNRS-IRISA in Rennes, France, since 2016. He was previously a postdoctoral researcher at the Italian Institute of Technology, Genova, Italy. Pacchierotti earned his PhD at the University of Siena in 2014. He was Visiting Researcher in the Penn Haptics Group at University of Pennsylvania in 2014, the Dept. of Innovation in Mechanics and Management at University of Padua in 2013, the Institute for Biomedical Technology and Technical Medicine (MIRA) at University of Twente in 2014, and the Dept. Computer, Control and Management Engineering of the Sapienza University of Rome in 2022. Pacchierotti received the 2014 EuroHaptics Best PhD Thesis Award and the 2022 CNRS Bronze Medal. He is Senior Chair of the IEEE Technical Committee on Haptics, Co-Chair of the IEEE Technical Committee on Telerobotics, and Secretary of the Eurohaptics Society.